

Atomic-scale nanofacet structure in semipolar (20 $\bar{2}$ 1) and (20 $\bar{2}$ 1) InGa \bar{N} single quantum wellsYuji Zhao^{1*}, Feng Wu¹, Tsung-Jui Yang², Yuh-Renn Wu², Shuji Nakamura¹, and James S. Speck¹¹Materials Department, University of California, Santa Barbara, CA 93106, U.S.A.²Institute of Photonics and Optoelectronics and Department of Electrical Engineering, National Taiwan University, Taipei 10617, Taiwan

E-mail: yujizhao@engineering.ucsb.edu

Received November 29, 2013; accepted January 10, 2014; published online January 29, 2014

Atomic-scale nanofacets were observed in semipolar (20 $\bar{2}$ 1) and (20 $\bar{2}$ 1) InGa \bar{N} quantum wells (QWs)/Ga \bar{N} quantum barriers interfaces. Transmission electron microscopy studies showed that these nanofacets were mainly composed of (10 $\bar{1}$ 0), (10 $\bar{1}$ 1), and (10 $\bar{1}$ 1) planes, which led to significant fluctuations in QW thickness. Atom probe tomography studies were carried out to visualize the nanofacet structure. The In composition in the In $_x$ Ga $_{1-x}$ N alloys followed a binominal distribution despite the formation of the nanofacet structure. One-dimensional (1D) Schrödinger–Poisson drift-diffusion simulation showed that these nanofacets and associated QW thickness fluctuations will lead to a large wavelength shift and a broadened spectral linewidth for semipolar QWs. © 2014 The Japan Society of Applied Physics

Nonpolar and semipolar III–nitride quantum wells (QWs) demonstrated great performance advantages for the fabrication of light-emitting diodes (LEDs) and laser diodes (LDs).¹⁾ One fundamental advantage of these novel orientations over the conventional polar *c*-plane structure is the elimination or reduction of polarization-related electric fields in the QW active region, which results in a significantly higher radiative recombination rate.^{2,3)} For this reason, several nonpolar and semipolar planes have been intensively investigated. Recently, InGa \bar{N} QWs on *m*-plane substrates with intentional miscut toward the *a*-direction have been demonstrated to have a longer wavelength and a narrower spectral linewidth than previous results, which are promising for device performance.⁴⁾ On the other hand, studies on semipolar planes have demonstrated great potential for high-efficiency devices.^{5,6)} For example, the semipolar (20 $\bar{2}$ 1) plane has been used to produce high-performance green LEDs and LDs.^{7,8)} It was argued that the residual-polarization-related electric field in (20 $\bar{2}$ 1) QW facilitated the long emission wavelength with low In compositions.⁹⁾ More recently, the semipolar (20 $\bar{2}$ 1) plane [which is the back side of the (20 $\bar{2}$ 1) plane that is crystallographically equivalent to the (20 $\bar{2}$ 1) plane] has attracted considerable attention for the demonstration of high-efficiency and low-droop blue LEDs.^{10–12)} The electric field was found to be almost zero for the (20 $\bar{2}$ 1) plane in diodes, which resulted in a high electron and hole wavefunction overlap and greatly reduced blue-shift.¹³⁾ Other advantages such as high In incorporation, high optical polarization, and narrow spectral linewidth (up to extremely high current densities) were also reported on (20 $\bar{2}$ 1) LEDs and LDs.^{14–18)} For green emitters, however, the stacking fault formation has limited device performance for both (20 $\bar{2}$ 1) and *m*-plane devices at around 490 to 500 nm.¹⁹⁾

Although much progress has been made in the device perspective, the underlying physics and material properties are still not well understood for these semipolar InGa \bar{N} QWs. Recent studies in hydride vapor phase epitaxy (HVPE) have shown that wurtzite Ga \bar{N} tends to form (0001), {10 $\bar{1}$ 1}, *m*-plane, and (000 $\bar{1}$) facets during the natural quasiequilibrium crystal growth, while neither the semipolar (20 $\bar{2}$ 1) nor (20 $\bar{2}$ 1) plane appears as a stable plane in unconstrained growth.^{20,21)} This potentially gives rise to the question on the atomic-scale structures of semipolar-based heterostructures, which not only affect the material properties but also have a significant impact on the carrier distribution and recombination process

for device operation.^{22,23)} An understanding of these atomic material properties on semipolar InGa \bar{N} QWs is therefore essential for the growth and fabrication of high-performance nitride-based optoelectronic devices. In this paper, we present the atomic structure of InGa \bar{N} QWs for semipolar (20 $\bar{2}$ 1) and (20 $\bar{2}$ 1) substrate orientations.

LED structures were grown by conventional metal organic chemical vapor deposition (MOCVD) on free-standing semipolar (20 $\bar{2}$ 1) and (20 $\bar{2}$ 1) Ga \bar{N} substrates supplied by Mitsubishi Chemical Corporation, with a threading dislocation density (TDD) on the order of 10⁵–10⁶ cm^{−2}. The miscut angles of the substrates were less than ±0.2° towards the [0001] and [1 $\bar{2}$ 10] directions. The substrates were treated by chemomechanical polishing to produce atomically flat surfaces with an RMS roughness of less than 1 nm. All growths were performed by MOCVD at atmospheric pressure with V/III ratios in excess of 3000 and in N₂ carrier gas. The device structure consisted of a 1 μm Si-doped n-Ga \bar{N} underlayer with a Si doping concentration of 1 × 10¹⁹ cm^{−3}, a 3 to 5 nm In_{0.24}Ga_{0.76}N single quantum well (SQW), a 3 to 10 nm Mg-doped Al_{0.15}Ga_{0.85}N electron-blocking layer (EBL) with a Mg concentration of 2 × 10¹⁹ cm^{−3}, and a 120 nm Mg-doped p-type Ga \bar{N} layer with a Mg concentration of 4 × 10¹⁹ cm^{−3}. For comparison, selective samples were grown with 15 sets of In_{0.05}Ga_{0.95}N/Ga \bar{N} superlattice (SL) underlayer before the SQW active region. The Ga \bar{N} layers were grown with trimethylgallium (TMGa) and ammonia (NH₃) precursors at a growth rate of ~10 Å/s and susceptor temperatures ranging from 980 to 1120 °C. The InGa \bar{N} SQW layer and SL underlayer were grown using triethylgallium (TEGa), trimethylindium (TMIn), and NH₃ precursors at a growth rate of ~1 Å/s and susceptor temperatures ranging from 750 to 820 °C. The target emission wavelengths for these devices were in the range from 480 to 520 nm. The devices show reasonable photoluminescence (PL) and electroluminescence (EL) intensities, indicating relatively good QW quality. Figure 1 shows the normalized EL spectra for (20 $\bar{2}$ 1) and (20 $\bar{2}$ 1) InGa \bar{N} SQW green LEDs emitting at around 515 nm, where the full width at half maximum (FWHM) for (20 $\bar{2}$ 1) SQW LEDs (~20 nm) is significantly smaller than that for (20 $\bar{2}$ 1) devices (~30 nm).

For material characterization, LED samples were studied by transmission electron microscopy (TEM), atom probe tomography (APT), and atomic force microscopy (AFM). The TEM and APT samples were prepared using a focused ion beam (FIB) with a Helios 600 dual-beam instrument.

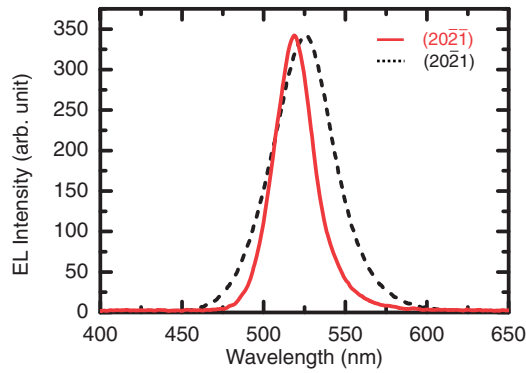


Fig. 1. Normalized EL spectra for $(20\bar{2}\bar{1})$ and $(20\bar{2}1)$ InGaN SQW green LEDs emitting at 515 nm.

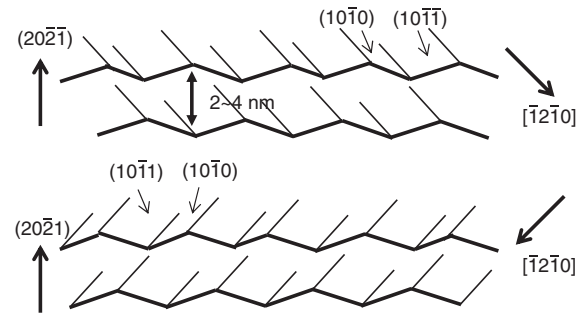


Fig. 3. Schematic views of nanofacets formed in $(20\bar{2}\bar{1})$ and $(20\bar{2}1)$ InGaN SQWs.

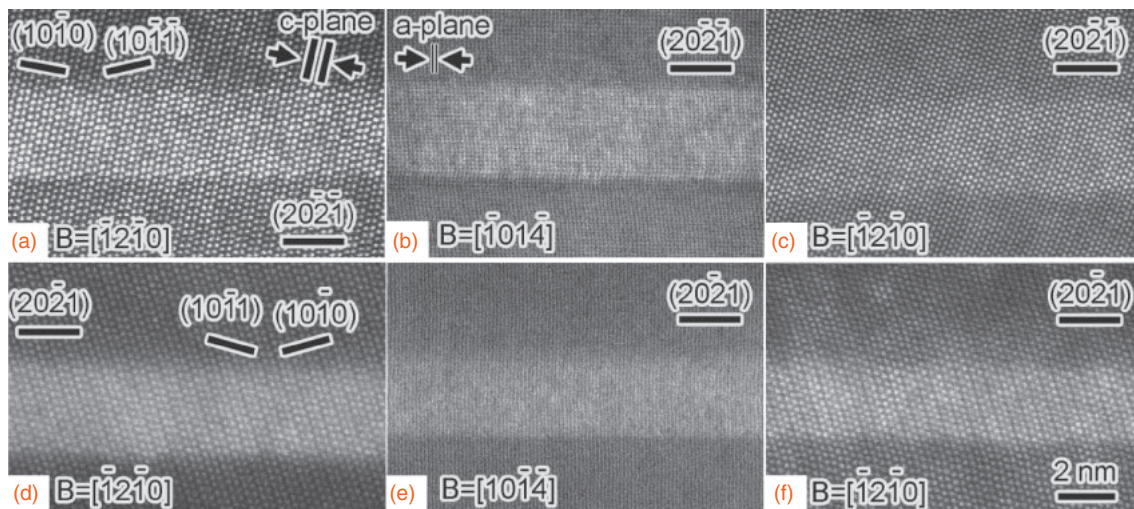


Fig. 2. HAADF images of $(20\bar{2}\bar{1})$ and $(20\bar{2}1)$ InGaN SQWs. (a, b) Images taken from the $(20\bar{2}\bar{1})$ InGaN SQW with 15 sets of $\text{In}_{0.05}\text{Ga}_{0.95}\text{N}/\text{GaN}$ SL underlayer, viewed along the $[\bar{1}2\bar{1}0]$ and $[\bar{1}01\bar{4}]$ directions, respectively. (c) $[\bar{1}2\bar{1}0]$ image taken from the $(20\bar{2}\bar{1})$ InGaN SQW without the InGaN/GaN SL underlayer. (d) $[\bar{1}2\bar{1}0]$ image of the $(20\bar{2}1)$ InGaN SQW with 15 sets of $\text{In}_{0.05}\text{Ga}_{0.95}\text{N}/\text{GaN}$ SL underlayer. (e, f) Images of the $(20\bar{2}1)$ InGaN SQW without the InGaN/GaN SL underlayer, viewed along $[\bar{1}01\bar{4}]$ and $[\bar{1}2\bar{1}0]$, respectively. Upward is the growth direction.

High-angle annular dark field (HAADF) images were taken with an FEI Titan FEG high-resolution TEM/STEM and analytical microscope, operated at 300 kV. The APT analysis was performed in laser mode with a Cameca Local Electrode Atom Probe 3000X HR at 30 K. The sample temperature was ~ 30 K. A simultaneous pulse of a Nd:YAG laser (532 nm second harmonic and 120 ps pulse width) at 250 kHz with a pulse energy of 0.06 nJ was used in the APT experiments. For reconstruction purposes, parameters were carefully chosen to demagnify the detector coordinates of the ions and give their specimen coordinates. Details of the APT methods can be found elsewhere.^{9,22)}

Figures 2(a)–2(f) demonstrate HAADF images for $(20\bar{2}\bar{1})$ and $(20\bar{2}1)$ InGaN SQW samples. Figures 2(a) and 2(c) are $[\bar{1}2\bar{1}0]$ cross-sectional images taken from $(20\bar{2}\bar{1})$ SQW samples with SLs [Fig. 2(a)] and without SLs [Fig. 2(c)], respectively. The HAADF images show that both the top and bottom surfaces of the InGaN SQW are composed of nanofacets, resulting in rough interfaces between the InGaN/GaN layers. The nanofacets are identified as $(10\bar{1}0)$ and $(10\bar{1}1)$ planes for $(20\bar{2}\bar{1})$ samples, as indicated in Fig. 2(a), and the facet features appear to be similar for samples with and without SL underlayers. The period of the zigzag facets is in

the range of 2 to 4 nm, and the amplitude of interface roughness is estimated to be less than 1 nm. The thickness fluctuation for the SQW is estimated to be 2 to 4 nm. Figure 2(b) shows the $[\bar{1}01\bar{4}]$ cross-sectional HAADF image for the $(20\bar{2}\bar{1})$ semipolar SQW samples with SLs. In contrast, the InGaN layer shows a flat interface in this direction. Similar atomic structures have been observed for semipolar $(20\bar{2}1)$ InGaN samples as shown in Figs. 2(d)–2(f). The facets on $(20\bar{2}1)$ samples have been identified as $(10\bar{1}0)$ and $(10\bar{1}1)$ planes. Compared with $(20\bar{2}\bar{1})$ samples, the $(20\bar{2}1)$ InGaN layer shows a rougher top surface in $[\bar{1}2\bar{1}0]$ cross-sectional images [Figs. 2(d) and 2(f)] and a more blurred image in the $[\bar{1}01\bar{4}]$ cross section [Fig. 2(e)]. Figure 3 demonstrates the schematic views for the nanofacets in both $(20\bar{2}\bar{1})$ and $(20\bar{2}1)$ InGaN SQWs. Owing to the facet formation, the SQW shows a rough surface and nonuniform thickness.

Figure 4 presents the APT results for both the $(20\bar{2}\bar{1})$ and $(20\bar{2}1)$ InGaN SQWs. Figure 4(a) shows the three-dimensional (3D) atom maps for two samples. Al, In, and Ga elements are labeled with yellow, blue, and purple, respectively, and the Al-rich AlGaIn layer and In-rich InGaN SQW layer can be identified from the 3D maps. It is noteworthy that a small amount of In was detected in the top GaN

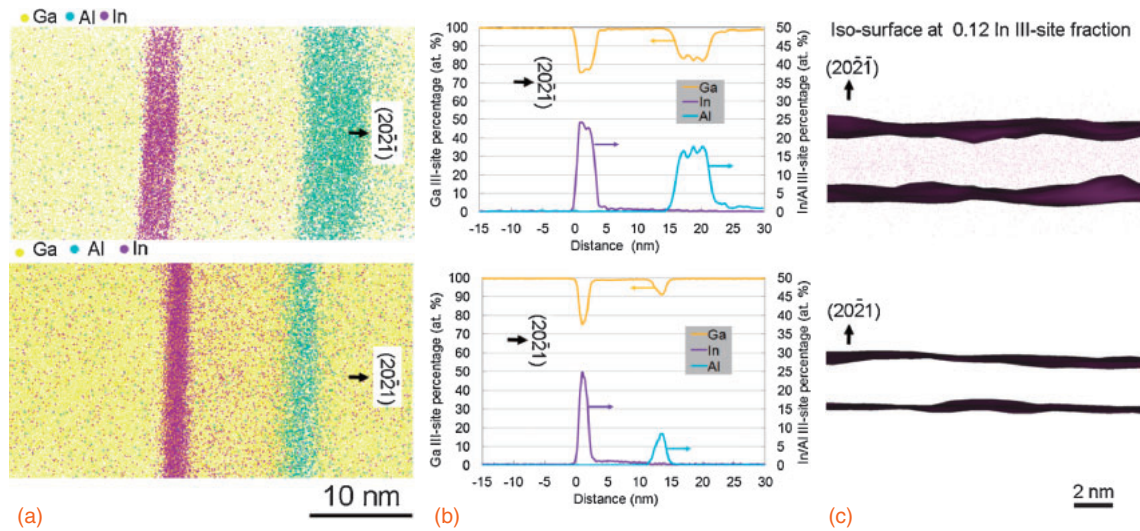


Fig. 4. (a) 3D atom probe images, (b) 1D proxigram analysis composition profile, and (c) isosurface for $(20\bar{2}1)$ and $(20\bar{2}1)$ InGaN SQW samples.

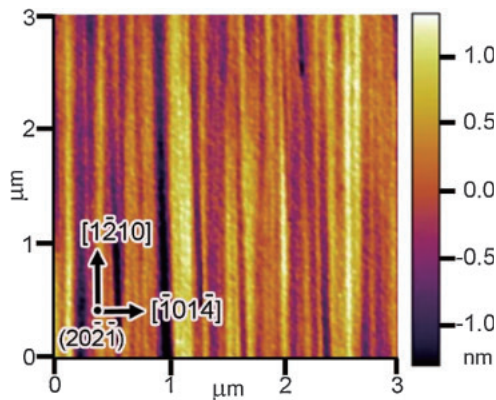


Fig. 5. AFM images for a $(20\bar{2}1)$ InGaN SQW sample.

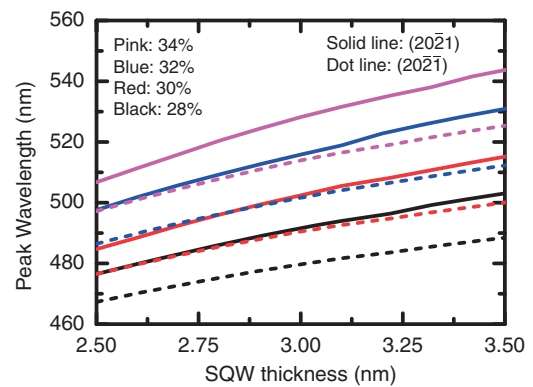


Fig. 6. Simulated peak wavelength as a function of SQW thickness for semipolar $(20\bar{2}1)$ and $(20\bar{2}1)$ SQWs with various In compositions.

quantum barrier layer for the $(20\bar{2}1)$ sample, possibly owing to the residual In incorporation on the $(20\bar{2}1)$ plane. Figure 4(b) shows the corresponding concentration profile for both the $(20\bar{2}1)$ and $(20\bar{2}1)$ samples with respect to the 0.1 iso-In III-site fraction surface. The In on both samples followed a binomial distribution, indicating that the materials are random alloys. The In III-site compositions were estimated to be $\sim 25\%$ for both structures. The $(20\bar{2}1)$ sample again shows a slightly longer tail for the In profile in the quantum barrier layer than the $(20\bar{2}1)$ sample, which is consistent with the 3D atom map results. Figure 4(c) shows the In iso-III-site fraction surface at 0.12. Both the $(20\bar{2}1)$ and $(20\bar{2}1)$ samples show rough surfaces, possibly owing to the observed faceting in TEM results. The $(20\bar{2}1)$ sample showed similar roughness for both the top and bottom interfaces, while for the $(20\bar{2}1)$ sample, the top interface is rougher.

Figure 5 shows the AFM image for an SQW $(20\bar{2}1)$ InGaN SQW sample. The striated morphology along the a -direction was observed for the sample. This striated feature on the surface is consistent with the general morphology of the nanofacets observed from the TEM study, which indicates that the atomic-scale nanofacets also have a significant impact on the surface morphology. It is also noteworthy that a similar morphology was observed for both $(20\bar{2}1)$ and $(20\bar{2}1)$ samples.

To further study the effects of nanofacets and the associated compositional and thickness fluctuations on device performance, calculations were carried out for a semipolar InGaN SQW. 1D Poisson drift-diffusion equations were solved self-consistently with different QW thicknesses and In compositions for different sections. Eigenstates and wave functions were then obtained by solving 1D Schrödinger equations for different QW thicknesses. The final emission spectrum might be the average result for different QW thickness regions. The polarization charges at the semipolar InGaN/GaN interface are determined using Ref. 24, and more details of the calculations can be found in Ref. 25. Figure 6 shows the simulated peak wavelength for $(20\bar{2}1)$ and $(20\bar{2}1)$ SQW LED structures with thickness fluctuation from 2.5 to 3.5 nm at different In compositions. When the SQW thickness increases, the simulated peak wavelength increases for the two planes. Owing to the larger residue-polarization-related electric field, the $(20\bar{2}1)$ devices showed longer emission wavelengths than the $(20\bar{2}1)$ devices, which is consistent with previous results.¹⁵⁾ This residual electric field leads to a stronger wavelength change on the $(20\bar{2}1)$ plane with respect to the SQW thickness fluctuation, which is evident from the larger slope for $(20\bar{2}1)$ curves (solid line) than for $(20\bar{2}1)$ curves (dot line). As a result, this nanofacet-induced thickness fluctuation will divide the QW region

into various emitting areas with different emitting wavelengths, which will lead to broadened spectra for the QW. The stronger impact on the (20 $\bar{2}$ 1) plane may result in a wider spectral linewidth on the device, which is observed in the experiment (Fig. 1). A more thorough study including 2D and 3D simulations is currently under way to fully understand this phenomenon.

In summary, we report the atomic-scale nanofacets in semipolar (20 $\bar{2}$ 1) and (20 $\bar{1}$) InGaN SQW LEDs. These nanofacets led to significant fluctuations in SQW thickness, which have significant impacts on the emission properties of semipolar QWs.

Acknowledgments The authors acknowledge the support of the Solid-State Lighting and Energy Center at UCSB. This work made use of Material Research Laboratory Central Facilities supported by the Materials Research Science and Engineering Centers Program of the National Science Foundation under Award No. DMR 1121053. The simulation work was partially funded by the National Science Council of Taiwan under grant No. NSC-102-2221-E-002-194-MY3.

- 1) S. Nakamura, *MRS Bull.* **34**, 101 (2009).
- 2) P. Waltereit, O. Brandt, A. Trampert, H. T. Grahn, J. Menniger, M. Ramsteiner, M. Reiche, and K. H. Ploog, *Nature* **406**, 865 (2000).
- 3) F. Bernardini and V. Fiorentini, *Phys. Status Solidi B* **216**, 391 (1999).
- 4) K. M. Kelchner, L. Y. Kuritzky, K. Fujito, S. Nakamura, S. P. DenBaars, and J. S. Speck, *J. Cryst. Growth* **382**, 80 (2013).
- 5) Y. Zhao, J. Sonoda, I. Koslow, C.-C. Pan, H. Ohta, J.-S. Ha, S. P. DenBaars, and S. Nakamura, *Jpn. J. Appl. Phys.* **49**, 070206 (2010).
- 6) Y. Zhao, J. Sonoda, C.-C. Pan, S. Brinkley, I. Koslow, K. Fujito, H. Ohta, S. P. DenBaars, and S. Nakamura, *Appl. Phys. Express* **3**, 102101 (2010).
- 7) Y. Enya, Y. Yoshizumi, T. Kyono, K. Akita, M. Ueno, M. Adachi, T. Sumitomo, S. Tokuyama, T. Ikegami, K. Katayama, and T. Nakamura, *Appl. Phys. Express* **2**, 082101 (2009).
- 8) S. Yamamoto, Y. Zhao, C.-C. Pan, R. B. Chung, K. Fujito, J. Sonoda, S. P. DenBaars, and S. Nakamura, *Appl. Phys. Express* **3**, 122102 (2010).
- 9) R. Shivaraman, Y. Kawaguchi, S. Tanaka, S. P. DenBaars, S. Nakamura, and J. S. Speck, *Appl. Phys. Lett.* **102**, 251104 (2013).
- 10) Y. Zhao, S. Tanaka, C.-C. Pan, K. Fujito, D. Feezell, J. S. Speck, S. P. DenBaars, and S. Nakamura, *Appl. Phys. Express* **4**, 082104 (2011).
- 11) C.-C. Pan, S. Tanaka, F. Wu, Y. Zhao, J. S. Speck, S. Nakamura, S. P. DenBaars, and D. Feezell, *Appl. Phys. Express* **5**, 062103 (2012).
- 12) C.-C. Pan, T. Gilbert, N. Pfaff, S. Tanaka, Y. Zhao, D. Feezell, J. S. Speck, S. Nakamura, and S. P. DenBaars, *Appl. Phys. Express* **5**, 102103 (2012).
- 13) D. F. Feezell, J. S. Speck, S. P. DenBaars, and S. Nakamura, *J. Disp. Technol.* **9**, 190 (2013).
- 14) Y. Zhao, Q. Yan, C.-Y. Huang, S.-C. Huang, P. S. Hsu, S. Tanaka, C.-C. Pan, Y. Kawaguchi, K. Fujito, C. G. Van de Walle, J. S. Speck, S. P. DenBaars, S. Nakamura, and D. Feezell, *Appl. Phys. Lett.* **100**, 201108 (2012).
- 15) Y. Zhao, S. H. Oh, F. Wu, Y. Kawaguchi, S. Tanaka, K. Fujito, J. S. Speck, S. P. DenBaars, and S. Nakamura, *Appl. Phys. Express* **6**, 062102 (2013).
- 16) C.-Y. Huang, Q. Yan, Y. Zhao, K. Fujito, D. Feezell, C. G. Van de Walle, J. S. Speck, S. P. DenBaars, and S. Nakamura, *Appl. Phys. Lett.* **99**, 141114 (2011).
- 17) Y. Zhao, S. Tanaka, Q. Yan, C.-Y. Huang, R. B. Chung, C.-C. Pan, K. Fujito, D. Feezell, C. G. Van de Walle, J. S. Speck, S. P. DenBaars, and S. Nakamura, *Appl. Phys. Lett.* **99**, 051109 (2011).
- 18) Y. Kawaguchi, C.-Y. Huang, Y.-R. Wu, Q. Yan, C.-C. Pan, Y. Zhao, S. Tanaka, K. Fujito, D. Feezell, C. G. Van de Walle, S. P. DenBaars, and S. Nakamura, *Appl. Phys. Lett.* **100**, 231110 (2012).
- 19) F. Wu, Y.-D. Lin, A. Chakraborty, H. Ohta, S. P. DenBaars, S. Nakamura, and J. S. Speck, *Appl. Phys. Lett.* **96**, 231912 (2010).
- 20) Q. Sun, C. D. Yerino, T. S. Ko, Y. S. Cho, I.-H. Lee, J. Han, and M. E. Coltrin, *J. Appl. Phys.* **104**, 093523 (2008).
- 21) B. N. Bryant, A. Hirai, E. C. Young, S. Nakamura, and J. S. Speck, *J. Cryst. Growth* **369**, 14 (2013).
- 22) Y.-R. Wu, R. Shivaraman, K.-C. Wang, and J. S. Speck, *Appl. Phys. Lett.* **101**, 083505 (2012).
- 23) Y. Zhao, F. Wu, C.-Y. Huang, Y. Kawaguchi, S. Tanaka, K. Fujito, J. S. Speck, S. P. DenBaars, and S. Nakamura, *Appl. Phys. Lett.* **102**, 091905 (2013).
- 24) A. E. Romanov, T. J. Baker, S. Nakamura, J. S. Speck, and ERATO/JST UCSB Group, *J. Appl. Phys.* **100**, 023522 (2006).
- 25) C.-P. Wang and Y.-R. Wu, *J. Appl. Phys.* **112**, 033104 (2012).